RSC Advances

ROYAL SOCIETY OF CHEMISTRY

www.rsc.org/advances

Biomimetic Fabrication of Robust Self-assembly Superhydrophobic Surfaces with Corrosion Resistance Properties on Stainless Steel Substrate

Tianchi Chen [a], Hongtao Liu [b]*, Haifeng, Yang [a], Wei Yan [b], Wei Zhu [b], Hao Liu [a]

[a] College of Mechanical & Electrical Engineering, [b] College of Materials Science and Engineering, China University of Mining and Technology, Xu Zhou, 221116, China

*Corresponding author: E-mail address: liuht100@126.com

Abstract: a reed leaf-like superhydrophobic stainless surface is obtained by nanosecond laser direct writing. Through investigating the coupling interaction between the laser fluence and the overlapping rate, we fabricate biomimetic reed leaf-like structures on the stainless steel. This biomimetic structures reveal excellent superhydrophobicity with a water contact angle of 157 ±1° and a sliding angle of 1 ± 0.5°after FAS-17 (1H, 1H, 2H, 2H-perfluorodecyltriisopropoxysilane) modification. The superhydrophobicity of the as-prepared surface results from its biomimetic hierarchical micro-nanostructure and the grafted low-surface-energy fluorosilane. The superhydrophobic surface exhibits high microhardness and excellent mechanical abrasion resistance. It can maintain superhydrophobicity after sandpaper abrasion against 260 grit Al_2O_3 sandpaper for 2.5 m at the applied pressure of 12.5 kPa. Moreover, the superhydrophobic surface has good chemical stability in both acidic and alkaline environments. The Tafel polarization curves show that the as-prepared superhydrophobic surface has better corrosion resistance than the bare stainless steel surface. It is believed that this stainless superhydrophobic surface may have important significance in the practical application.

Keywords: superhydrophobic, laser process, anti-abrasion, corrosion resistance.

1. Introduction

Inspired by the lotus[1], rice leaf[2], butterfly wing[3], salvinia leaf[4], and water-strider legs[5], many scholars design a number of functional interfacial materials with superwettability. Low-adhesive superhydrophobic surface is defined as a surface with a water contact angle larger than 150° and a slide angle less than 10°. Such surfaces are highly expected to be widely used in many fields, such as self-cleaning[6], anti-icing[7], anti-corrosion[8], oil−water separation[9] and drag reduction[10]. Up to now, many researcher investigated that low surface energy and hierarchical structures are two main factors to achieve superhydrophobic surface. According to above-mentioned factors of achieving superhydrophobic surface, many methods have been realized in surface roughness, such as electrochemical methods[11, 12], Sol−Gel methods[13], spin-coating methods[14], spray methods[15] and chemical vapor deposition[16]. However, all above methods exist some problems, such as the

adhesion between coating and substrate or preparation stability. The micro structures generated by laser direct writing are original structures without consideration of the adhesion between coating and substrate, and the laser direct writing system have been proven that it is a simple and effective way to obtain hierarchical micro/nano structures in the micro-fabrication field[17] due to structure controllability, non-pollution and localization manufacture. The laser can easily process steels[18], silicon[19], and polymers[20]. Thus, many superhydrophobic surfaces have been successfully fabricated by laser direct writing. For instance, Cardoso [21] used 70-ps pulses laser to prepare square-shaped pillars superhydrophobic polymeric surface. Luo[22] also used a short pulse excimer laser to prepare quare-shaped pillars on the 316L stainless steel surface and then deposit amorphous carbon coatings on the prepared surface, the coating surface acquired a water contact angle of 150°. Wohl [23] used YAG laser with a wavelength of 355nm to ablate low surface energy copoly (imide siloxane)s. Laser-etched square pillar arrays (25 μm pillars with 25 μm interspaces) changed contact angles from 111° to 175°. Sun et al[24] successfully prepared a water contact angle of 163° ± 1° on silicon wafers with different regular patterns fabricated by utilizing the excimer laser. Vorobyev[25] used femtosecond laser pulses to produce multifunctional superhydrophobic metal surface with the hierarchical pillar structure or grating structure. Wu[26] used femtosecond laser pulses to fabricate periodic ripples and periodic cone-shaped spikes covered with superhydrophobic laser-induced periodic surface structure on the stainless steel, and the maximal apparent contact angle reached 166.3°. However, most of above-mentioned reports used the high-cost, low efficiency, complex femto-/pico-second lasers to prepare superhydrophobic surface. Nanosecond laser is a compact, cost–effective and high manufacturing efficiency device, which has been proved as an effective tool for surface-texture processing. Boinovich [27-29] used nanosecond laser with the wavelength of 1064nm to fabricate series of superhydrophobic surfaces on the stainless steel and aluminum alloy substrates. Ta[30] also used laser with the wavelength of 1064nm to fabricate series of superhydrophobic surfaces on the copper substrates. The most of research selected infrared laser to fabricate superhydrophobic surface. However, the ultraviolet nanosecond laser is rarely used to fabricate superhydrophobic surface. Due to the smaller wavelength, the surface ablated by ultraviolet nanosecond laser has less heat effect area than that of infrared laser. Thus, the ultraviolet nanosecond laser easily fabricate hierarchical structures. And most of materials can absorb ultraviolet ray, which mean that ultraviolet nanosecond laser can process more kinds of materials than infrared laser. Moreover, as it follows from the literature, the infrared laser ablated surface needs to UV treatment to enriching the surface with hydroxyl groups. For the ultraviolet laser, the surface can absorb the ultraviolet ray during the laser processing, which can realize the laser processing and surface hydroxylation at the same time.

One of the problem limiting the scientific and industrial application of superhydrophobic surface is its weak mechanical abrasion resistance. Some superhydrophobic surfaces are easily failure owing to a slight scratch or the abrasion by sandpaper, even the finger contact. Besides, anticorrosion properties are equally crucial for practical outdoor use, especially for the natural marine environment, which mainly depends on the surface chemical composition and surface structures. Varieties of methods have been developed to improve the corrosion resistance, such as some polymer nanocomposites coatings[31-34]. However, achieving anti-corrosion superhydrophobic surface directly on the metal surface is still a great challenge. As mentioned above, stainless steel, one of the most important engineering material owing to its excellent anti-corrosion ability and mechanical properties, is chosen as a research object in our work to in order to achieve superhydrophobic surface with both good mechanical abrasion resistance and chemical stability. Stainless steel is widely used in many applications such as pipes, outer wall decoration material and heat exchangers on the corrosive environment. Thus, many researchers have fabricated various superhydrophobic surface on the stainless steel. Liu[35] prepared superhydrophobic binary microstructures on the stainless steel surface by the chemical etching. Zhang[36] successfully obtained the superhydrophobic flaky γ-alumina film on the 316L stainless steel with a contact angle for water of 152°. Motlagh [37] utilized spray coating to fabricate superamphiphobic coatings on stainless steel and the fabricated coating had long-period durability and high corrosion resistance. However, most of literatures reveal that stainless steel is only used as a substrate, which can be replaced by other metal materials.

From the above analysis, it can be concluded that excellent mechanical abrasion and corrosion resistance can enlarge the application of the metal-based superhydrophobic surfaces. Herein, a facile laser direct writing method is used to obtain the superhydrophobic surface on the stainless steel. In this work, a systematic research investigated relationship between laser powers, scanning spaces and wettability. More importantly, Not only do prepared surface exhibits outstanding superhydrophobic performance, but also has superior mechanical abrasion resistance, chemical stability, corrosion resistance, which has an important significance in the practical application of superhydrophobic surface.

2. Experiment Sections

2.1 Materials

In this paper, we selected 316L type austenitic stainless steel pieces with size of 20×20 mm and thickness of 1 mm. The sample was mechanically polished, then rinsed with deionized water, degreased by a 30 min ultrasonic bath in acetone, dried in a dry box. FAS-17(1H, 1H, 2H,

2H-perfluorodecyltriisopropoxysilane) (97%) was purchased from SICONG chemical.

2.2 Fabrication of stainless steel superhydrophobic surface

The dried samples were irradiated by a 25 ns ultraviolet laser with a working wavelength of 355nm，repetition rate of 6.8 kHz. A laser marker with a focus lens (*f*=160mm) was used to control the focused laser beam in the x-y direction. The radius of beam waist of the laser pulses after the focusing lens was approximately 18μm. The laser scanning trajectory was firstly line-by-line in x direction then in y direction. In our experiments, the laser powers were changed from 57.5 mW to 1111.7 mW. The laser scanning intervals were varied from 20μm to 100μm. The laser scanning speed was fixed at 5.28mm/s. After laser processing experiment, samples were cleaned with distilled water and dried at 60 °C for 1h. Finally, the samples were immersed into 2 wt% FAS-17(1H, 1H, 2H, 2H-perfluorodecyltriisopropoxysilane) ethanol solution for 1h followed by washing with ethanol and drying in an oven at 100 °C for 1h.

2.3 Characterizations

Surface morphologies of all the samples were investigated using a scanning electron microscope (FEI limited, Quanta 250). The sample chemical compositions were characterized by an Energy Dispersive Spectrum (EDS, Bruker). The water contact angle (CA) and sliding angle were measured with 5 μL deionized water droplet dripped on the five different points for each surface using the JC2000D-2A contact angle measuring device. The sample surface roughness was characterized with a Bruker's Dektak XT stylus profilers.

The mechanical abrasion resistance of as-prepared sample was evaluated by tape-peeling, sharp-scratch, and sandpaper abrasion tests. The mechanical stability of as-prepared surface was firstly investigated qualitatively by tape-peeling. The adhesive force by tape would destroy fragile micro structures, making the touched area permanently lose its superhydrophobicity. Then the sharp-scratch test was used to evaluate whether our superhydrophobic surface can maintain its superhydrophobicity after sharp object scratched on the surface. Finally, sandpaper abrasion test was related to large area abrasion or wear. The prepared surface was loaded with different load, facing 260 grid Al_2O_3 sandpaper surface as an abrading surface, moved different distance at a fixed velocity of 4~8cm/s.

The chemical stability and corrosion resistance of superhydrophobic surface were carried out in chemical stability test and electrochemical corrosion test. The chemical stability test was used to perform the relationship between superhydrophobicity of as-prepared surface and acidic/alkaline environments. Samples immersed into acidic or alkaline solution for different hours. The contact angles and sliding angles were measured after samples were taken out from the

solution and dried at 60 °C oven. Electrochemical corrosion test was carried out in a three electrode cell. An as-prepared surface, a platinum plate and saturated calomel electrode (SCE) were used as the working electrode, counter and reference electrode, respectively. The polarization curve was measured in 3.5wt % NaCl solution by an electrochemical workstation (RST5000). Before the electrochemical corrosion test, the surface area of the test samples immersed into the corrosion solution was 1 cm^2 for 30 min. Salt fog test, to some extent, is similar to the natural marine environment. Here, the salt fog test is according to ASTM B117 and prior reference[38]. Firstly, the specimens were mounted between 15 and 30° from vertical and preferably parallel to the principle direction of the fog flow in the chamber. There would be 1.5±0.5 mL collected solution per hour for each 80 cm^2 of the horizontal collecting area. The salt solution was prepared by 5 wt% NaCl solution. The pH of the collected solution was from 6.5 to 7.2. The temperature of the salt spray chamber was maintained at 35 ± 2 °C.

3. Results and discussion

3.1 Superhydrophobic Surface Morphology and its Formation Mechanism

Figure. 1 shows SEM images of reed leaf surface at different magnifications. As can be seen in Fig. 1, reed leaf surface has lots of micro scale ridge structures which has the length larger than 40 μm and width of 15 μm and some micro scale mastoids with the diameter of 10μm. The micro scale ridge structures cover with lots of nano scale protuberances with diameter of about 200 nm and height of 6μm. A lot of air exist in the space between these micro/nano hierarchical structures, which enables the reed leaf surface to have the superhydrophobic properties.

In order to obtain reed leaf-like structures, we firstly investigate the influence of laser processing parameters on the surface morphologies. We divide processing parameters into two series: A series is to investigate the influence of laser powers on the surface morphologies and B series is to reveal the changes in surface morphologies by varying laser scanning intervals. In A series, samples were irradiated by varying laser powers from 57.5 mW to 1111.7 mW at the fixed laser scanning velocity of 5.28 mm/s and laser scanning interval of 20μm. In B series, the laser scanning intervals were changed from 20μm to 100μm at the fixed laser power of 1111.7 mW and laser scanning velocity of 5.28 mm/s.

Figure.2 shows changes in surface morphology with gradually increasing of laser powers. The laser-processed surfaces (A1-A8) reveal significant difference by comparison of that of the unprocessed surface (A0). At the relative lower laser power, such as samples A1 and A2, surface morphology changes a little and maintains flat. There are only few craters with size of 5-10μm

random distributed and some re-melting ripple structures on the surface. With laser power continuously increasing, some nano or micro particles appear on the edge of laser scanning path and the period of micro-particles decrease with laser powers. Surprisingly, this grating structure just like the ridge structures of reed leaf is fabricated by suitable laser powers from 221.4 mW to 366.6 mW, such as samples A3-A5. When the laser power increase to 568.3 mW, the surface structures suddenly change to transition state structures including microcavities and microprotrusions (A6). With laser powers continuously increasing, melting microprotrusions form micro-strip structures with length around 80μm and the depth of microcavity increases. Moreover, there are many nano structures gradually appearing on the micro structures from the high-magnification level SEM images on samples A7-A8. With the comparison of SEM images between the reed leaf (Figure.1) and Sample A7 or A8, it can be found that the as-prepared surface is structural similar to reed leaf surface in a certain degree.

Figure. 3 shows the influence of laser scanning intervals on the surface morphology. Some interesting phenomena have been discovered from SEM images of B series. Firstly, when the laser scanning space is larger than the diameter of laser beam waist diameter, the processed surfaces reveal regular pillars or holes, as shown in samples B2-B5. Moreover, some nano/micro particles are founded at the edge of laser scanning area. This also proves that laser power is a key parameter in the preparation of biomimetic hierarchical structures. When the laser scanning spaces is less than the diameter of beam waist, the processed surface reveals self-assembled biomimetic hierarchical structures, as shown in B1.

As discussed above, the generation of biomimetic hierarchical structure needs to the synergy of laser powers and laser scanning intervals. Generally, the distribution of laser fluence is in concordance with the Gaussian distribution, its fluence profile can be expressed as:

$$\Phi_{(r)} = \Phi_0 e^{\frac{-2r^2}{w_0^2}} \quad (1)$$

where, Φ_0 is the peak fluence of laser beam. w_0 is the radius of beam waist which means the radius at the *1/e* of laser peak fluence. *r* is the radius from laser beam centerline. The peak fluence of laser beam, Φ_0 is directly related to laser power and laser pulse repetition frequency. The expression of Φ_0 can be written as:

$$\Phi_0 = \frac{2P}{f\pi w_0^2} \quad (2)$$

where, *P* is the laser average power. *f* is the laser pulse repetition frequency.

When the nanosecond laser pulse irradiates on the surface, the target surface absorbs a large amount of heat. Due to its long pulse period, there is enough time for the thermal wave to propagate into the target and to create a relatively large heat-effected metal layer[39]. At the lower

laser pulse fluence, with local temperature increase on the irradiated region, the melting area firstly occurs on the metallic material surface. Then evaporation occurs from the melting metal surface. Thus, the laser ablation only causes melting and evaporation of metal surface. The depth of the removed material in the ablated area is about tens of nanometers. The ablated rate of is very slow, which depends on the optical penetration depth[40], and the ablated area is to be smooth[41]. Some re-melting structures appear on the surface, such as A1-A2. With the increase of laser fluence, when the surface temperature increase to some breakpoint, a large amount of vaporization nucleus appear under the melting materials surface. When the steam pressure on the melting material is greater than surface tension of melting liquid, the melting materials begin to ejecting away from center of laser beam. Meanwhile, the recoil pressure on the melted surface results in the formation of a micro-cavity[42]. Moreover, Electrons around the irradiated region easily form plasma in the high laser fluence[43]. The plasma would interfere the energy absorption of the ablated surface and make the splashing droplet re-deposited on the ablated region[44]. This can well explain the phenomenon that some nano/micro particles are formed at the edge of laser scanning area in samples B3, B4 and B5. Thus, the form of laser ablation are existing in vaporization and phase explosion, the ablated rate grows rapidly by the increasing laser power, the depth of removed materials per pulse is of the order of hundreds of nanometers and the surface becomes rougher[40]. The minimal laser fluence required to initially ablate the material is called the 'gentle' ablation threshold. Laser ablation just above 'gentle' ablation threshold is called 'gentle' ablation. The minimal laser fluence required to occur vaporization and phase explosion is called 'strong' ablation threshold. Laser ablation just above 'strong' ablation threshold is called 'strong' ablation.

According to equation (1) and (2), the diameter of gentle ablation and strong ablation area can be expressed as follow:

$$D_i^2 = 2w_0^2(lnP + ln\frac{2}{f\pi w_0^2\varphi_i}) \quad (3)$$

Where *Di* is the diameter of laser ablation area, subscript *i* means types of ablation: gentle ablation and strong ablation area. w_0 is the radius of beam waist. *P* is the laser average power. *f* is the laser pulse repetition frequency. φ_i is the 'gentle' material surface ablation threshold or the 'strong' material surface ablation threshold.

Figure. 4 (a) shows theoretical diameters of laser ablation areas with different laser powers. The inset of Figure. 4 (a) shows the schematic illustration of different diameters of laser beam, including the 'gentle' laser ablation diameter, 'strong' laser ablation diameter and laser beam waist diameter. For the 'strong' laser ablation, the laser ablation diameters at laser power over 568.3 mW are larger than laser diameter waist. Combing the SEM images at different powers, we find

that the surface reveals hierarchical structures when the 'strong' laser ablation diameter is equal or larger than laser diameter waist, otherwise the surface reveals micro grating structures. Figure. 4 (b) shows a histogram that visually demonstrates the ratio of laser ablation area to laser beam waist area at different laser powers. It can be seen that for the 'gentle' laser ablation, laser ablation areas are almost greater than laser beam waist areas at all the experimental laser powers; for the 'strong' laser ablation, only when the laser power is higher than 568.3 mW, the 'strong' laser ablation region has a larger area than laser beam waist region. According to the theoretical diameter of the 'strong' laser ablation and the laser scanning space of 20μm, two typical laser spot overlapping situations are shown in Figure. 4 (c). When the laser ablation diameter is larger than laser scanning space, three laser spots can overlap in the x direction. When the laser ablation diameter is less than laser scanning space, three laser spots overlap in pairs in the x direction. The laser spot overlapping rate in x direction are calculated and shown in Figure. 4 (d). When the 'strong' laser ablation overlapping rate is much less than the overlapping rate of laser beam waist diameter, for instance samples A3-A5, the repetition area is smaller and the distance between the repetition areas is also far away from each other. Hence, grating structures with some nano or micro particles appearing on the edge of laser scanning path are achieved at the samples A3-A5. As the 'strong' laser ablation overlapping rate increasing with laser powers, the size of microparticle increases with laser powers. So the distances between repetition areas are gradually closer. When the 'strong' laser ablation area is close to the laser beam waist area, some microcavities and large area of microbumps begin to form owing to the overlap between 'strong' laser ablation areas. Sample A6 reveals a transition structure from micrograting structure to hierarchical structure. When the 'strong' laser ablation area is over the laser beam waist area, a large area of random distributed microcavities and microparticle structures appear on the surface. It should be noted that the self-assembled reed leaf-like hierarchical structures would not change much and only the difference is that the size of microparticle and the depth of microcavity increase with laser powers, as shown in samples A7-A8.

3.2 Wettability

The rough surface is successfully constructed by laser processing. Then a low surface energy material (FAS-17) is grafted on the as-prepared surface. A series of the EDS spectra at 5000× magnification are presented in Figures S1 in the SI. Contrasting to the chemical composition on the un-grafted surface, the Si, C, F and O elements, the major elements of FAS-17, are detected on all the grafted samples. Fig. 5 (a) reveals the XPS survey spectrum of the as-prepared superhydrophobic surface. The presence of Si, C, F and O elements on the superhydrophobic surface can be observed. Fig. 5 (b) shows the C1s decomposition-fitted curves of the XPS spectra.

The C1s peaks locating at 293.63eV and 291.22 eV are assigned to the carbon atom of $-CF_3$ and $-CF_2-$, respectively. The peaks at 288.50 eV and 284.49 are assigned to carbon atom of $-CH_2-CF_2-$ and -C-C-. The peak at 281.95 eV is attributed to the carbon atom of −C−Si. The XPS results indicate that FAS-17 was successfully grafted onto the specimen surface. The formation mechanism of the self-assembled FAS-17 molecular film on the rough laser processed surface has been widely discussed due to the fact that hydrolysed FAS-17 molecules react with the −OH groups of the laser processed surface and crosslink among adjacent hydrolysed FAS-17 molecules []. FAS-17 molecule can effective reduce the surface energy of the laser processed surface depending on its $-CF_3$ group with a surface energy of 6.7 mJ/m^2 and $-CF_2$ group with a surface energy of 18 mJ/m^2.

Figure. 6 (a) shows that the unprocessed surface is hydrophobic because of its water contact angle around 95°. The water contact angle increases with laser powers. After the laser power reaches to 366 mW, the water contact angle is stable around 155°. The sliding angle has a same result, as shown in Figure. 6 (a) (Samples, A series). The sample has an ultra-low sliding angle of 3° when the laser power is over 366mw, which means as-prepared surface has an excellent water repellent property. Figure. 6 (b) shows the relation between laser scanning spaces and water contact angles or sliding angle (Samples, B series). All the samples appear similar superhydrophobicity, their water contact angles are greater than 150° and sliding angles is less than 5°. Generally, there are two classic model used to describe the interface between rough surface and liquid: (1) In the Wenzel model[45], the water completely infiltrated the rough surface; (2) In the Cassie model[46], the air is existing between the liquid and solid phases. In our experiment, when laser power is low, the smaller contact and larger sliding angle can be explained according to the Wenzel model, as shown in Figure. 7 (a). When the laser power increases to 366 mW, the surface shows superhydrophobicity with large contact angle and low sliding angle, which can be explained by the Cassie model, as shown in Figure. 7 (b). Because of a large roughness consisting of reed leaf-like microbumps and deep micropores combined with rich nanostructures, air can be easily trapped between the surface structure and droplet, which causes the interruption of a three-phase solid-water-air contact line[47]. Thus, this leads to ultra-excellent water repellent property and an extremely low water adhesion. In order to further validate the mechanism of superhydrophobicity of our samples, we observe the side view and the overlook view of interface between liquid and our sample surface. From the top view, it can be clearly seen that the white area is the air bubbles and the black area is mainly comprised of microstructure and water. Most of microstructures are filled with air bubbles, as shown in Figure. 7 (c). As shown in Figure. 7 (d), from the side view, the white air layer can be clearly observed between droplet and

microstructures, which proves that Cassie model are suitable to explain the mechanism of superhydrophobicity in our samples.

Surface roughness profile curves are shown in Figure S2 to further explain the relationship between surface morphology and wetting behavior for these samples. Figure. S3 shows that there is a gradual increase for roughness with sample number. The roughness is in agreement with the observation of surface morphology, which has three typical roughness regions. In the flat structure region, the unprocessed surface has an average surface roughness about 83nm. After laser treatment at the lower laser power, their profile curves are smooth and the roughness of samples A1 and A2 slightly increases to 165.19nm and 403.72nm, respectively. The water contact also increases from 95° to 121°. In the micro-grafting structures region, the profile curves of samples A3-A5 have average roughness around 3300nm. The distance between peak and valley is around 8000nm. Their contact angles of samples A3-A5 are around 150°. As the laser power increasing, when the 'strong' laser ablation diameter is close to or more than the laser beam waist diameter, biomimetic hierarchical structures appear on the processed surface, as shown in samples A6-A8. Owing to the hierarchical structure, their roughness are greater than 5000nm. The distance between peak and valley is around 20000nm, which is the important factor to result in the sufficient air pockets trapped in the surface.

3.3 Mechanical abrasion

It is essential for superhydrophobic surface to have a good anti-abrasion property for the practical application. Tape-peeling, sharp-scratch, and sandpaper abrasion tests are used to estimate the anti-abrasion property of as-prepared superhydrophobic surface. The tape-peeling can make a great damage to fragile micro structures, which causes a decline in surface superhydrophobicity[48]. As shown in Video S1, a water droplet are still a sphere on the touched surface and can easily roll off at a small tilting angle, which proves that our sample remains the excellent superhydrophobicity after tape-peeling for several times. The surface are often scratched by some sharp objects, such as knife, needle and tweezer in our daily life. Sharp-scratch test is used to exam whether our superhydrophobic surface can maintain superhydrophobicity after random scratch on the sample A8. A schematic view of the sharp-scratch test is shown in Figure. 8 (a). A tweezer is used to scratch superhydrophobic sample A8 along the path of black lines to test the surface robustness. The optical image of scratched surface among with images of contact angle and sliding angle are present in Figure. 8 (b). The contact angle and sliding angle of the scratched sample A8 are 154° and 4°, respectively. The mirror-like phenomenon is viewed at the interface between the droplet and sample surface from the optical image of scratched surface. The cause of mirror-like effect is the existence of a thin air layer between water and the superhydrophobic

surface[49]. Sandpaper abrasion tests have been reported to evaluate the mechanical abrasion resistance of the superhydrophobic surfaces by many researchers[48, 50, 51]. In this work, a schematic view of the sandpaper abrasion test is shown in Figure. 9 (a). The 260 grit Al_2O_3 sandpaper is used as a friction surface. The superhydrophobic sample A8 facing the sandpaper at the different applied pressures and abrasion distances. Figure. 9 (b) shows that the contact angle decreases and sliding angle increase after abrasion for 2.5 m at 12.5 kPa. Finally, the water drops maintains a spherical shape with a contact angle of 152° and a sliding angle of 10°, as shown in video S2. These above results reveal that the as-prepared superhydrophobic surface has an excellent superhydrophobicity. After comparing other reported metal superhydrophobic surface[48, 51-54], we find that the as-prepared surface shows a better mechanical stability. For instance, the Ag/polymer superhydrophobic surface endure abrasion for 30 cm at an applied pressure of 10.0 kPa[48]; the sliding angle of superhydrophobic Si surface increased significantly from 1°to 70° after 25cm of abrasion on a Technicloth wipe surface under 3.45 kPa pressure[51]; the superhydrophobicity on the magnesium alloy surface disappeared after 70cm of abrasion under 1.2 kPa pressure[53]; a superhydrophobic copper surface was failure after abrasion for 1.0 m at a pressure of 6.0 kPa on 800 grid sandpaper[52]; a superhydrophobic aluminum alloys surface could only be abraded 90 cm at a pressure of 10kPa on 2000 grid sandpaper[54]. Compared to above-mentioned superhydrophobic surface, the hardness of as-prepared surface displays a micro hardness of 429.7 ± 5 $kgf \cdot mm^{-2}$, which is much higher than the bare stainless steel of 166.5 ± 5 $kgf \cdot mm^{-2}$. This high hardness can provide a solid foundation for anti-abrasion of our superhydrophobic materials.

Figure. 10 shows SEM images of the abraded superhydrophobic surface after abrasion 1.0 m and abrasion 2.5 m at the applied pressure of 12.5 kPa. The peak part of microstructure is worn by sandpaper with the comparison of original superhydrophobic sample A8 surface. The new surface generated by abrasion is still hierarchical structure, but the abrasion process would reduce the height of microstructure and increase the distance between microstructures. Thus, the rough hierarchical structure still exists. Figure. S4 shows chemical components of sample before/after abrasion 2.5 m at the applied pressure of 12.5 kPa. The Si, C, F and O elements, the major elements of FAS-17, are still detected on the abraded sample, which indicating that FAS-17 still exists on the new generated structure. Table. S1 shows the quantitative analysis result of chemical compositions of sample before/after abrasion. After abrasion, the Si, C, F and O elements experience a downward trend. The content of F element slightly decrease from 15.74% to 13.77%. The existence of FAS-17 and new generated microstructure are two main reason for the exhibition of superhydrophobicity. Furthermore, the past reports [52-54] only introduce the results of sandpaper abrasion test, but ignore the influence of different superhydrophobic structures on anti-abrasion

ability. Thus, we perform a sandpaper abrasion test on the regular pillar superhydrophobic samples (B2-B5) and the sample B1 (hierarchical micro-nanostructures). Figure. 9(c) presents contact angle and sliding angles of different structures superhydrophobic surface after abrasion 2.5 m at the applied pressure of 12.5 kPa. It can be clear seen that the contact angle decreases and sliding angle increase for all the tested samples. It is important to point out that the contact angles of samples B2-B5 greatly decrease to less than 145° and the sliding angles greatly increase to more than 10° after abrasion 2.5 m at the applied pressure of 12.5 kPa. The hierarchical micro-nanostructures reveal better hydrophobicity than regular pillar superhydrophobic structures after sand paper abrasion test. Figure. S5 shows SEM images of the abraded different structures superhydrophobic surface after abrasion 2.5 m at the applied pressure of 12.5 kPa. Compared to the superhydrophobic surface containing hierarchical micro-nanostructures, the regular pillar superhydrophobic surface has a larger broken area. The nanostructure around the edge of pillar is almost worn. The pillar structures gradually change to hole-array structures. It is worth noting that the sliding angle of sample B2 is bigger than sample B3. This is mainly due to the fact that the hole-array structures are not obvious after sandpaper abrasion on the sample B2 when intervals between pillars are too narrow. The water droplet contact more structures than that of B3. Surface roughness profile curves of samples B series before/after abrasion are shown in Figure S6 (a) and (b). Figure. S6(c) is a histogram of surface roughness of samples B series before/after abrasion. After abrasion, the surface roughness decreases for the B series samples. Thus, the loss of large area of micro/nanostructure could be a reason for the decline of sliding angle. The quantitative analysis results of chemical compositions of samples before/after abrasion 2.5 m at the applied pressure of 12.5 kPa are shown in Table. S2. The contents of Si, C, F and O greatly decrease after abrasion in the sample B2-B5. Moreover, the content of F element of sample B1-B5 are 6%, 1.54%, 2.38%, 1.65%, 1.08% and the changes of contact angle and sliding angle of are consist with the changes of F and C elements. For both surface morphology and FAS-17 content, biomimetic hierarchical micro-nanostructures (sample B1) display a better superhydrophobicity after abrasion than regular pillar structures (sample B2-B5). This is due to the fact that the biomimetic hierarchical structure including microcavities and reed leaf-like microstructures can be grafted by more fluorosilane and the broken surface area is relatively small during the course of friction, the exposed areas are replenished by sufficient fluorosilane molecules [55]. Thereby, fluorosilane molecules provide healing of the abraded surface. For the regular pillar structure, the fluorosilane molecules only graft on the surface of pillar, which means that the storage of fluorosilane is less than hierarchical micro-nanostructures. The broken area is relatively large in the sandpaper test. Thus, there are not sufficient fluorosilane molecules providing healing of the

abraded surface, which cause the greatly decreasing of hydrophobicity.

3.4 Chemical Stability and Corrosion Resistance

Many materials often fails in some acidic and alkaline environments. In this study, the pH value of the solution is adjusted by hydrochloric acid (0.5 M HCl) or sodium hydroxide (1 M NaOH). Figure. 11 shows the variation of the water contact angle and sliding angle against time duration. The as-prepared surface maintains superhydrophobicity in both of acidic or alkaline solution after 24h immersion. The contact angle is still above 150° and the sliding angle is less than 10°, which reveals that as-prepared superhydrophobic surface has good chemical stability in both acidic and alkaline environments. It is mainly due to the fact that the hydrophobic agent (FAS-17) chemically reacted with −OH groups on the as-prepared surface, which is more stable than that of physically absorbed hydrophobic agent such as perfluoropentadecane and docosane [28]. The decreasing of hydrophobicity is mainly contributed by the slightly hydrolysis of -O-Si- in a layer of self-assemble chemisorbed FAS-17 molecules. Hence, the as-prepared superhydrophobic surface possesses good chemical stability in both acidic and alkaline environments.

The Tafel polarization curves of bare stainless steel, unmodified laser processed sample and FAS-17 modified superhydrophobic sample are carried out to measure their corrosion potential and corrosion current in 3.5 wt% NaCl solution. As shown in Figure. 12 (a) and Table. S3, it can be noting that the superhydrophobic surface has better anti- corrosion ability than bare stainless steel because it has higher corrosion potential (E_{corr}=169.9mV) and lower corrosion current ($I_{corr}=3.16\times10^{-9}A/cm^2$) with comparison of bare stainless steel surface (E_{corr}=292.4mV and $I_{corr}=5.01\times10^{-7}A/cm^2$) and unmodified surface (E_{corr}=304.4mV and $I_{corr}=2.51\times10^{-7}A/cm^2$). The above results show that the superhydrophobic surface has a good corrosion protection for the stainless steel and laser processed surface has equal corrosion resistance to that of bare stainless steel. Figure. 12 (b) shows Tafel curves of as-prepared superhydrophobic surface at different immersion times in the 3.5 wt% NaCl solution. Table. S4 gives the E_{corr} and I_{corr} extrapolated from the Tafel curves. The E_{corr} did not change much after 168h immersion and eventually shifted to 161.9mV, indicating the good chemical stability of the superhydrophobic surface in a corrosive environment over a long immersion time. I_{corr} slightly increases to $6.31\times10^{-9}A/cm^2$ after 168h 3.5 wt% NaCl solution immersion. But I_{corr} is still reduced by more than 2 order of magnitude for the superhydrophobic surface in comparison with the untreated stainless steel surface. Compared to other metal surfaces such as carbon steel[56], magnesium alloy[57] and copper[58], stainless steel has inherent anti-corrosion ability, and on this basis, superhydrophobic stainless steel surface makes better corrosion resistance due to the fact that the air layer trapped in biomimetic roughness microstructures can form an air protective layer, which can prevent NaCl solution penetrating into

the micro−nano hierarchical structures and reduce the real contact area between NaCl solution and roughness microstructures[8].

Salt fog test is to evaluate corrosion resistance in the natural marine environment. Figure. 13 shows the optical image of as-prepared superhydrophobic surface before/after 120h corrosion test with spraying salt fog. After exposing the superhydrophobic surface to the salt fog for 120 h, the sample have not the obvious outward appearance change. The contact angle is still around 157°。This observation further confirms that our prepared superhydrophobic surface has a better corrosion resistance.

4. Conclusion

Superhydrophobic surfaces were prepared by nanosecond laser process. By controlling laser parameters: laser powers and laser scanning spaces, we successfully fabricated three typical microstructures including flat structure, micro-grating structure and biomimetic hierarchical micro/nano structure. The change of different microstructures can be concluded as coupling interaction between the laser fluence and overlapping rate of laser beam radius. After modified with FAS-17, biomimetic hierarchical micro/nano structures reveal excellent water repellence with water contact angle of 157° and sliding angle of 1°. The superhydrophobic mechanism is due to special biomimetic hierarchical micro/nano structure and low surface energy material, which construct an air layer between the surface and the water droplet. The as-prepared superhydrophobic surface has high hardness, excellent mechanical abrasion resistance, and excellent chemical stability in both acidic and alkaline environments as well as outstanding corrosion resistance in 3.5 wt % NaCl solution. Hence, this robust, chemical stability and corrosion resistance stainless superhydrophobic surface may have important significance in the practical application.

Acknowledge

This work was supported by the National Nature Science Foundation of China (No.51475457), Qing Lan Project, the China Postdoctoral Science Foundation Funded Project (Grant No. 2015M581881) and A Project Funded by the Priority Academic Program Development of Jiangsu Higher Education Institutions.

References

1. B. Bhushan, Y. C. Jung, A. Niemietz and K. Koch, *Langmuir*, 2009, **25**, 1659-1666.
2. L. Feng, S. Li, Y. Li, H. Li, L. Zhang, J. Zhai, Y. Song, B. Liu, L. Jiang and D. Zhu, *Advanced materials*, 2002, **14**, 1857-1860.
3. Y. Zheng, X. Gao and L. Jiang, *Soft Matter*, 2007, **3**, 178-182.

4. C.-Y. Yang, Y.-L. Tsai, C.-Y. Yang, C.-K. Sung, P. Yu and H.-C. Kuo, *Applied Physics Express*, 2014, **7**, 087001.
5. X. Gao and L. Jiang, *Nature*, 2004, **432**, 36-36.
6. R. Fürstner, W. Barthlott, C. Neinhuis and P. Walzel, *Langmuir*, 2005, **21**, 956-961.
7. A. Kim, C. Lee, H. Kim and J. Kim, *ACS applied materials & interfaces*, 2015, **7**, 7206-7213.
8. J. Ou, W. Hu, M. Xue, F. Wang and W. Li, *ACS applied materials & interfaces*, 2013, **5**, 3101-3107.
9. J. Li, L. Shi, Y. Chen, Y. Zhang, Z. Guo, B.-l. Su and W. Liu, *Journal of Materials Chemistry*, 2012, **22**, 9774-9781.
10. R. J. Daniello, N. E. Waterhouse and J. P. Rothstein, *Physics of Fluids (1994-present)*, 2009, **21**, 085103.
11. H. Liu, X. Wang and H. Ji, *Applied Surface Science*, 2014, **288**, 341-348.
12. B. Zhang, X. Zhao, Y. Li and B. Hou, *RSC Advances*, 2016, **6**, 35455-35465.
13. Y. Tang, Q. Zhang, X. Zhan and F. Chen, *Soft matter*, 2015, **11**, 4540-4550.
14. C. K. Söz, E. Yilgör and I. Yilgör, *Polymer*, 2015, **62**, 118-128.
15. J. Li, L. Yan, H. Li, J. Li, F. Zha and Z. Lei, *RSC Advances*, 2015, **5**, 53802-53808.
16. S. Rezaei, I. Manoucheri, R. Moradian and B. Pourabbas, *Chemical Engineering Journal*, 2014, **252**, 11-16.
17. F. Chen, D. Zhang, Q. Yang, J. Yong, G. Du, J. Si, F. Yun and X. Hou, *ACS applied materials & interfaces*, 2013, **5**, 6777-6792.
18. A.-M. Kietzig, S. G. Hatzikiriakos and P. Englezos, *Langmuir*, 2009, **25**, 4821-4827.
19. J. Yong, Q. Yang, F. Chen, D. Zhang, H. Bian, Y. Ou, J. Si, G. Du and X. Hou, *Applied Physics A*, 2013, **111**, 243-249.
20. J. Yong, Q. Yang, F. Chen, D. Zhang, G. Du, H. Bian, J. Si and X. Hou, *RSC Advances*, 2014, **4**, 8138-8143.
21. M. Cardoso, V. Tribuzi, D. Balogh, L. Misoguti and C. Mendonça, *Applied Surface Science*, 2011, **257**, 3281-3284.
22. B. Luo, P. W. Shum, Z. Zhou and K. Li, *Surface and Coatings Technology*, 2010, **204**, 1180-1185.
23. C. J. Wohl, M. A. Belcher, L. Chen and J. W. Connell, *Langmuir*, 2010, **26**, 11469-11478.
24. C. Sun, X.-W. Zhao, Y.-H. Han and Z.-Z. Gu, *Thin Solid Films*, 2008, **516**, 4059-4063.
25. A. Vorobyev and C. Guo, *Journal of Applied Physics*, 2015, **117**, 033103.
26. B. Wu, M. Zhou, J. Li, X. Ye, G. Li and L. Cai, *Applied Surface Science*, 2009, **256**, 61-66.
27. L. B. Boinovich, A. M. Emelyanenko, A. D. Modestov, A. G. Domantovsky and K. A. Emelyanenko, *ACS applied materials & interfaces*, 2015, **7**, 19500-19508.
28. L. Boinovich and A. Emelyanenko, *Colloids and Surfaces A: Physicochemical and Engineering Aspects*, 2015, **481**, 167-175.
29. A. M. Emelyanenko, F. M. Shagieva, A. G. Domantovsky and L. B. Boinovich, *Applied Surface Science*, 2015, **332**, 513-517.
30. D. V. Ta, A. Dunn, T. J. Wasley, R. W. Kay, J. Stringer, P. J. Smith, C. Connaughton and J. D. Shephard, *Applied Surface Science*, 2015, **357**, 248-254.
31. J. Liu, J. Huang, E. K. Wujcik, B. Qiu, D. Rutman, X. Zhang, E. Salazard, S. Wei and Z. Guo, *Macromolecular Materials and Engineering*, 2015, **300**, 358-368.
32. H. Wei, D. Ding, S. Wei and Z. Guo, *Journal of Materials Chemistry A*, 2013, **1**, 10805-10813.
33. C. Yang, H. Wei, L. Guan, J. Guo, Y. Wang, X. Yan, X. Zhang, S. Wei and Z. Guo, *Journal of Materials Chemistry A*, 2015, **3**, 14929-14941.
34. H. Wei, Y. Wang, J. Guo, N. Z. Shen, D. Jiang, X. Zhang, X. Yan, J. Zhu, Q. Wang and L. Shao, *Journal of Materials Chemistry A*, 2015, **3**, 469-480.
35. Y. Liu, Y. Bai, J. Jin, L. Tian, Z. Han and L. Ren, *Applied Surface Science*, 2015, **355**, 1238-1244.
36. X. Zhang, X. Liu, J. Laakso, E. Levänen and T. Mäntylä, *Applied Surface Science*, 2012, **258**, 3102-3108.
37. N. V. Motlagh, F. C. Birjandi, J. Sargolzaei and N. Shahtahmassebi, *Applied Surface Science*, 2013, **283**, 636-647.
38. J. Zhu, S. Wei, I. Y. Lee, S. Park, J. Willis, N. Haldolaarachchige, D. P. Young, Z. Luo and Z. Guo, *Rsc Advances*, 2012, **2**, 1136-1143.
39. B. Chichkov, C. Momma, S. Nolte, F. Von Alvensleben and A. Tünnermann, *Applied Physics*

A, 1996, **63**, 109-115.
40. W. Wang, X. Mei, G. Jiang, S. Lei and C. Yang, *Applied Surface Science*, 2008, **255**, 2303-2311.
41. C. McDaniel, A. Flanagan and G. M. O'Connor, *Applied Surface Science*, 2014, **295**, 1-7.
42. M. Gubko, A. Ionin, S. Kudryashov, S. Makarov, A. Rudenko, L. Seleznev and D. Sinitsyn, *JETP letters*, 2013, **97**, 599-603.
43. N. Bloembergen, *Quantum Electronics, IEEE Journal of*, 1974, **10**, 375-386.
44. J. Kido, H. Hayase, K. Hongawa, K. Nagai and K. Okuyama, *Applied physics letters*, 1994, **65**, 2124-2126.
45. R. N. Wenzel, *The Journal of Physical Chemistry*, 1949, **53**, 1466-1467.
46. A. Cassie and S. Baxter, *Transactions of the Faraday Society*, 1944, **40**, 546-551.
47. C. Extrand and S. I. Moon, *Langmuir*, 2012, **28**, 15629-15633.
48. X. Zhu, Z. Zhang, X. Men, J. Yang, K. Wang, X. Xu, X. Zhou and Q. Xue, *Journal of Materials Chemistry*, 2011, **21**, 15793-15797.
49. I. A. Larmour, S. E. Bell and G. C. Saunders, *Angewandte Chemie*, 2007, **119**, 1740-1742.
50. Y. Lu, S. Sathasivam, J. Song, C. R. Crick, C. J. Carmalt and I. P. Parkin, *Science*, 2015, **347**, 1132-1135.
51. Y. Xiu, Y. Liu, D. W. Hess and C. Wong, *Nanotechnology*, 2010, **21**, 155705.
52. J. Ou, W. Hu, S. Liu, M. Xue, F. Wang and W. Li, *ACS applied materials & interfaces*, 2013, **5**, 10035-10041.
53. Z. She, Q. Li, Z. Wang, L. Li, F. Chen and J. Zhou, *Chemical Engineering Journal*, 2013, **228**, 415-424.
54. Y. Zhang, D. Ge and S. Yang, *Journal of colloid and interface science*, 2014, **423**, 101-107.
55. H. Jin, X. Tian, O. Ikkala and R. H. Ras, *ACS applied materials & interfaces*, 2013, **5**, 485-488.
56. L. Boinovich, S. Gnedenkov, D. Alpysbaeva, V. Egorkin, A. Emelyanenko, S. Sinebryukhov and A. Zaretskaya, *Corrosion Science*, 2012, **55**, 238-245.
57. T. Ishizaki, Y. Masuda and M. Sakamoto, *Langmuir*, 2011, **27**, 4780-4788.
58. L. Feng, L. Zhao, X. Qiang, Y. Liu, Z. Sun and B. Wang, *Applied Physics A*, 2015, **119**, 75-83.

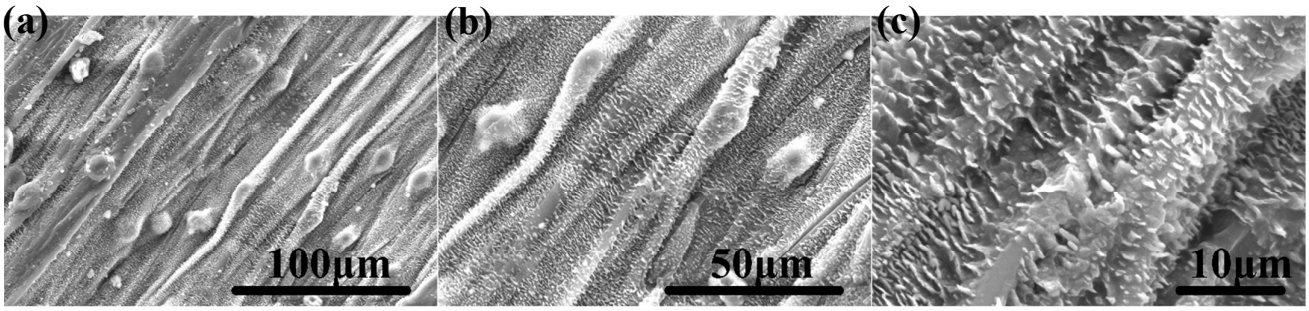

Figure.1 The SEM images of the reed leaf at different magnifications, (a) ×500, (b) ×1000, (c) ×3000.

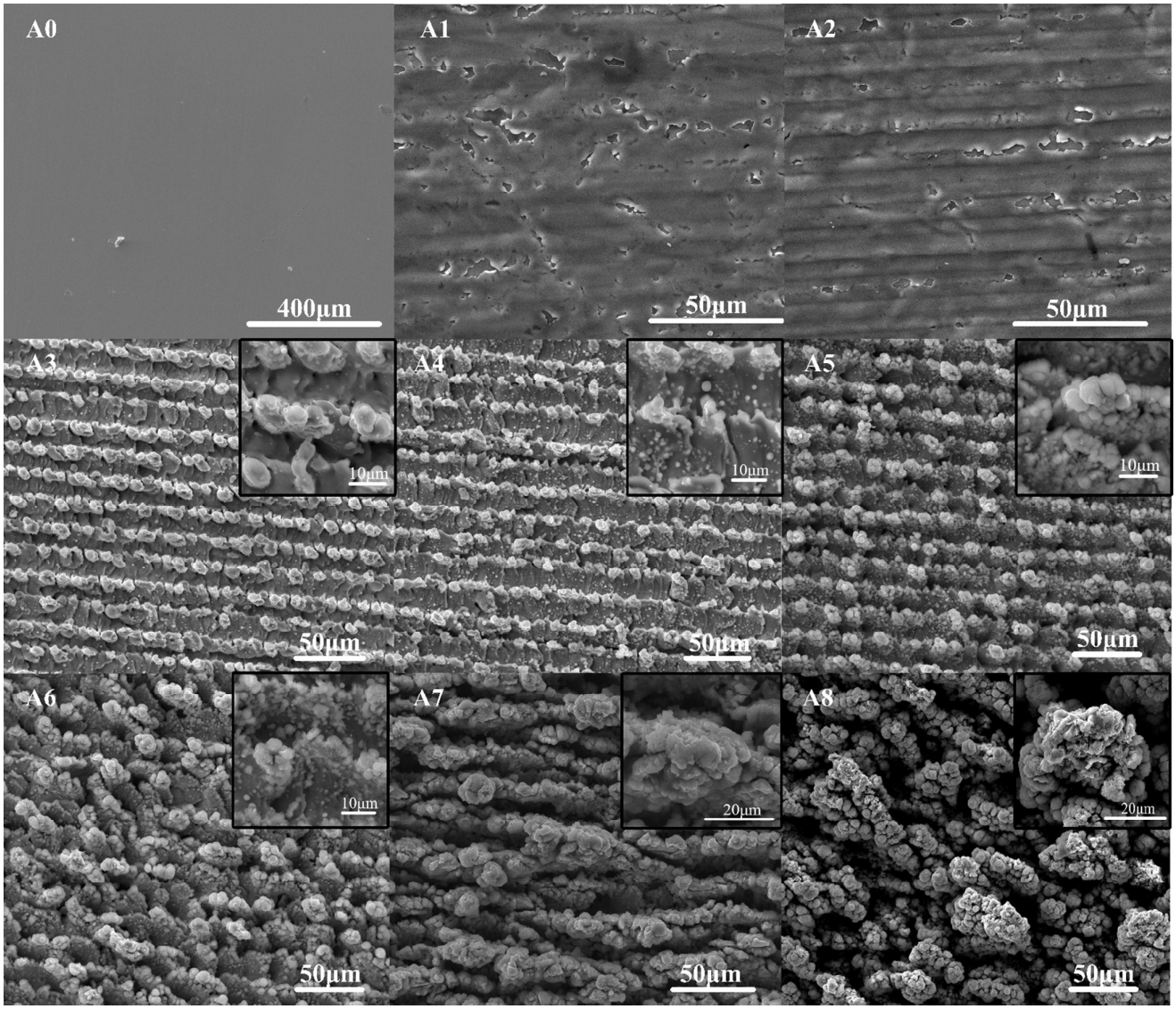

Figure.2 SEM images of the stainless steel surface under different laser powers, A0: 0 mW, A1: 57.5 mW, A2:86.0 mW, A3: 221.4 mW, A4: 299.3 mW, A5:366.6, A6: 568.3 mW, A7: 831.5 mW, A8: 1111.7 mW.

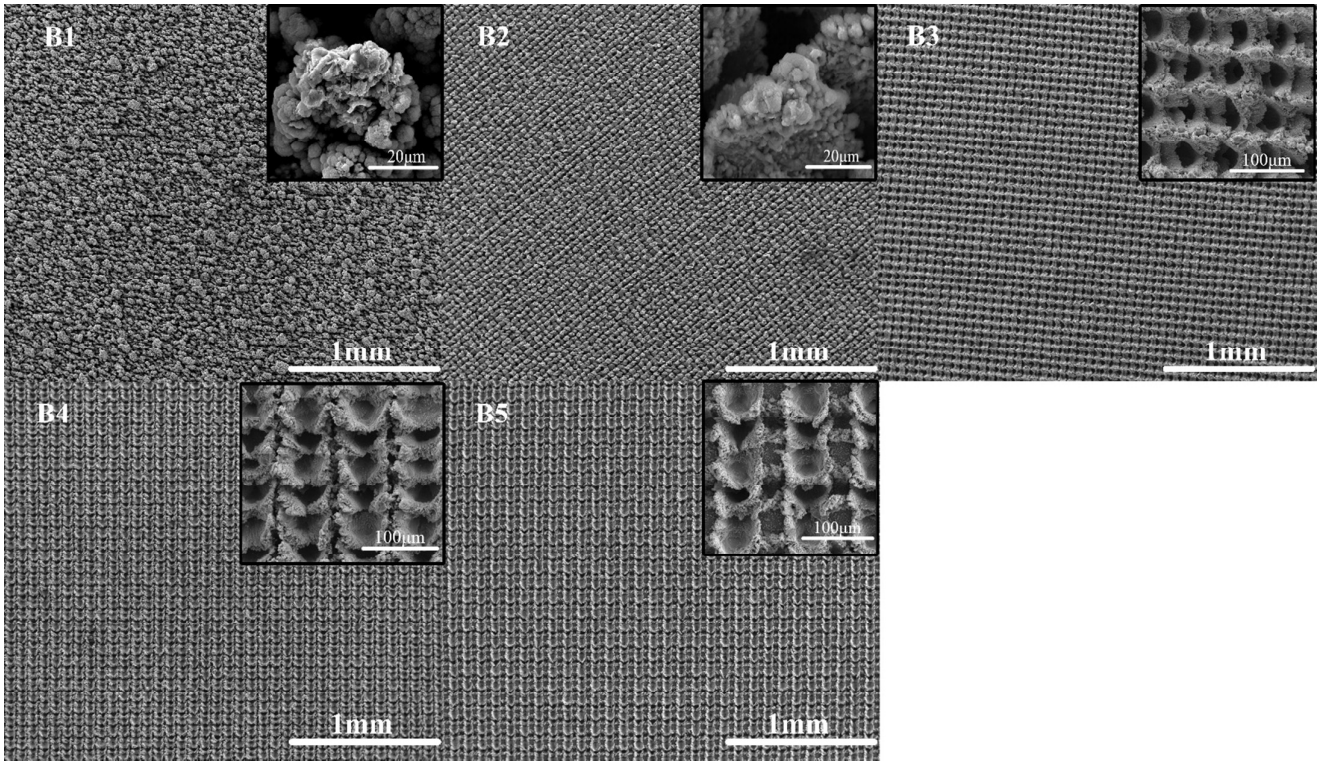

Figure.3 SEM images of the stainless steel surface under different laser scanning spaces, B1: 20 μm, B2: 40 μm, B3: 60 μm, B4: 80 μm, B5: 100 μm.

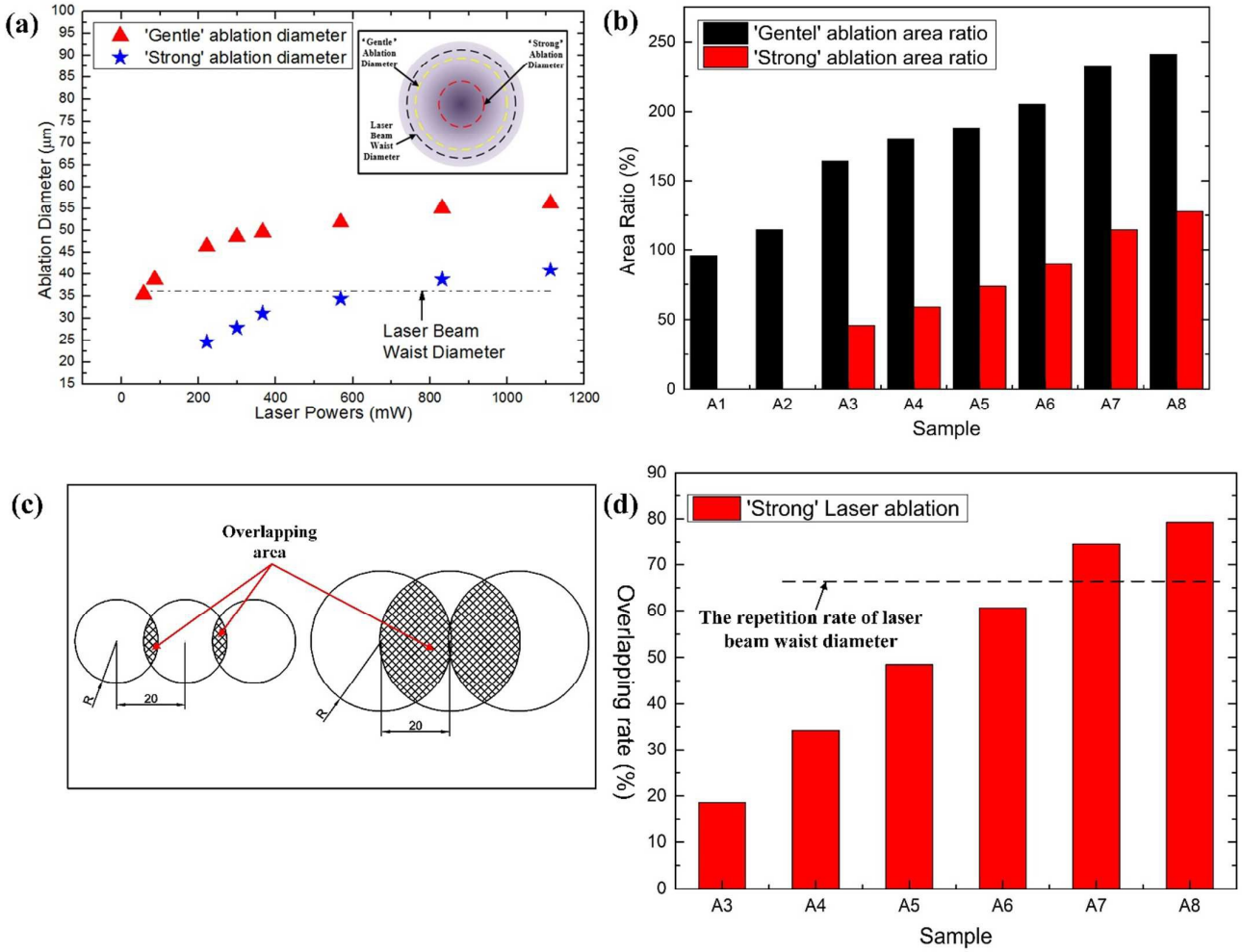

Figure. 4. The relationship between laser ablation diameters and laser powers, (a) ablation diameter, (b) area ratio, (c) the schematic diagram of overlapping area, (d) overlapping rate.

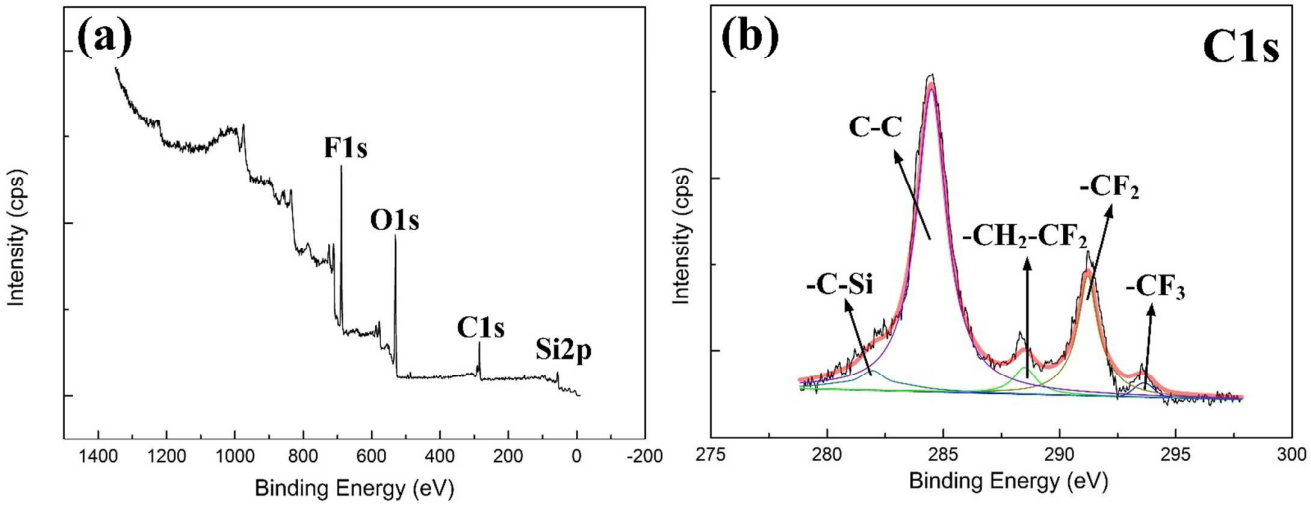

Figure. 5 XPS spectra of the superhydrophobic surface: (a) XPS survey spectra, (b) high-resolution of C1s.

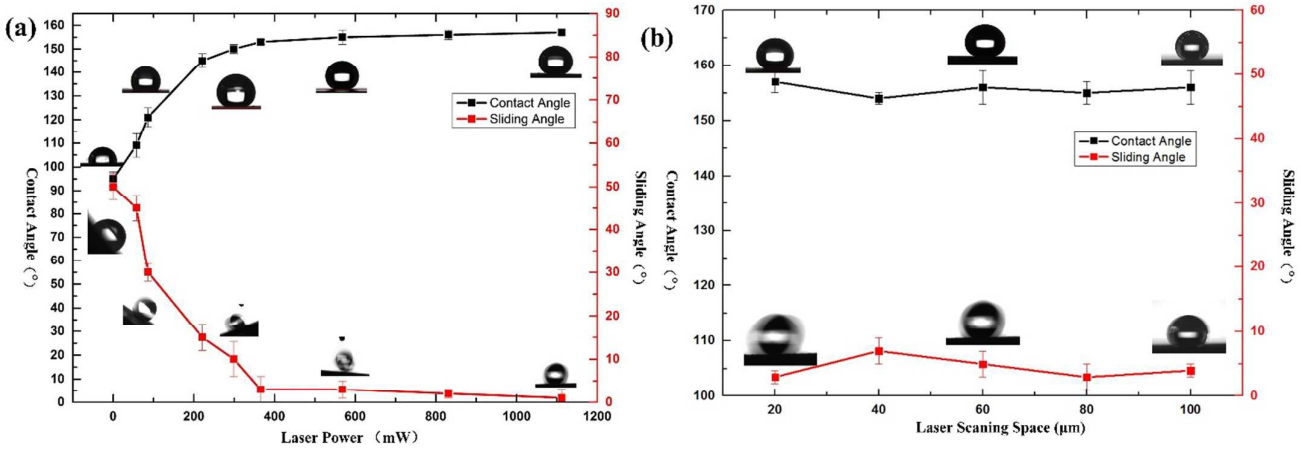

Figure. 6 The contact angles and sliding angles of different laser parameters, (a) laser powers, (b) laser scanning spaces

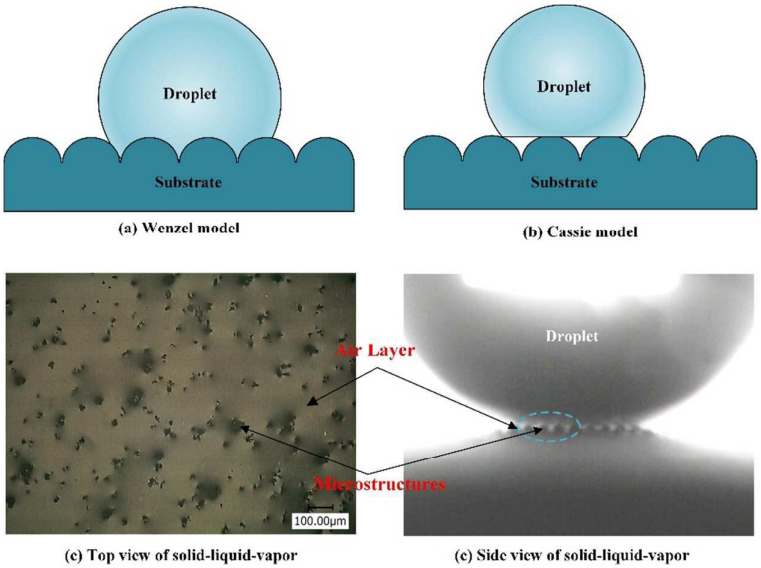

Figure .7 The superhydrophobic mechanism of as-prepared surface, (a) Wenzel model, (b) Cassie model, (c) top view of solid-liquid-vapor, (d) side view of solid-liquid-vapor.

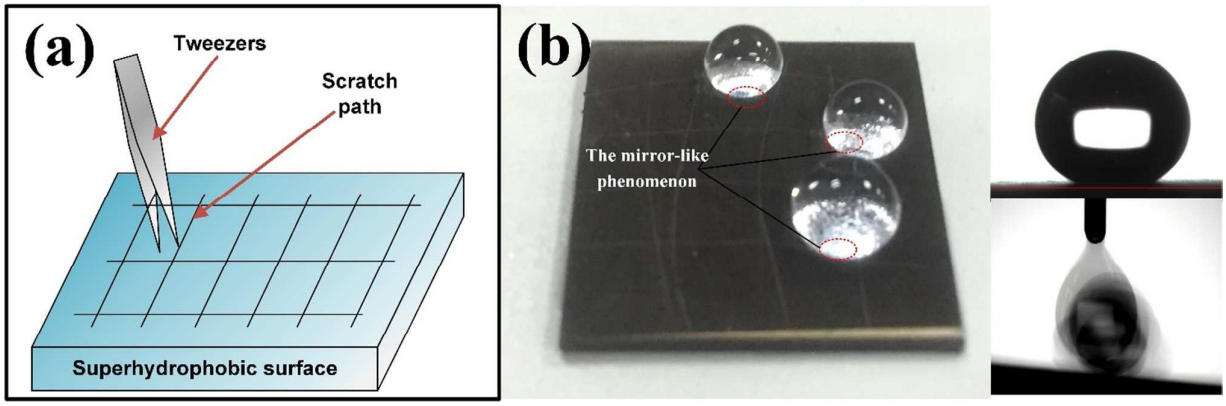

Figure 8. (a) Illustration of the sharp-scratch test for A8 surface, (b) Wetting behavior of A8 after the abrasion test.

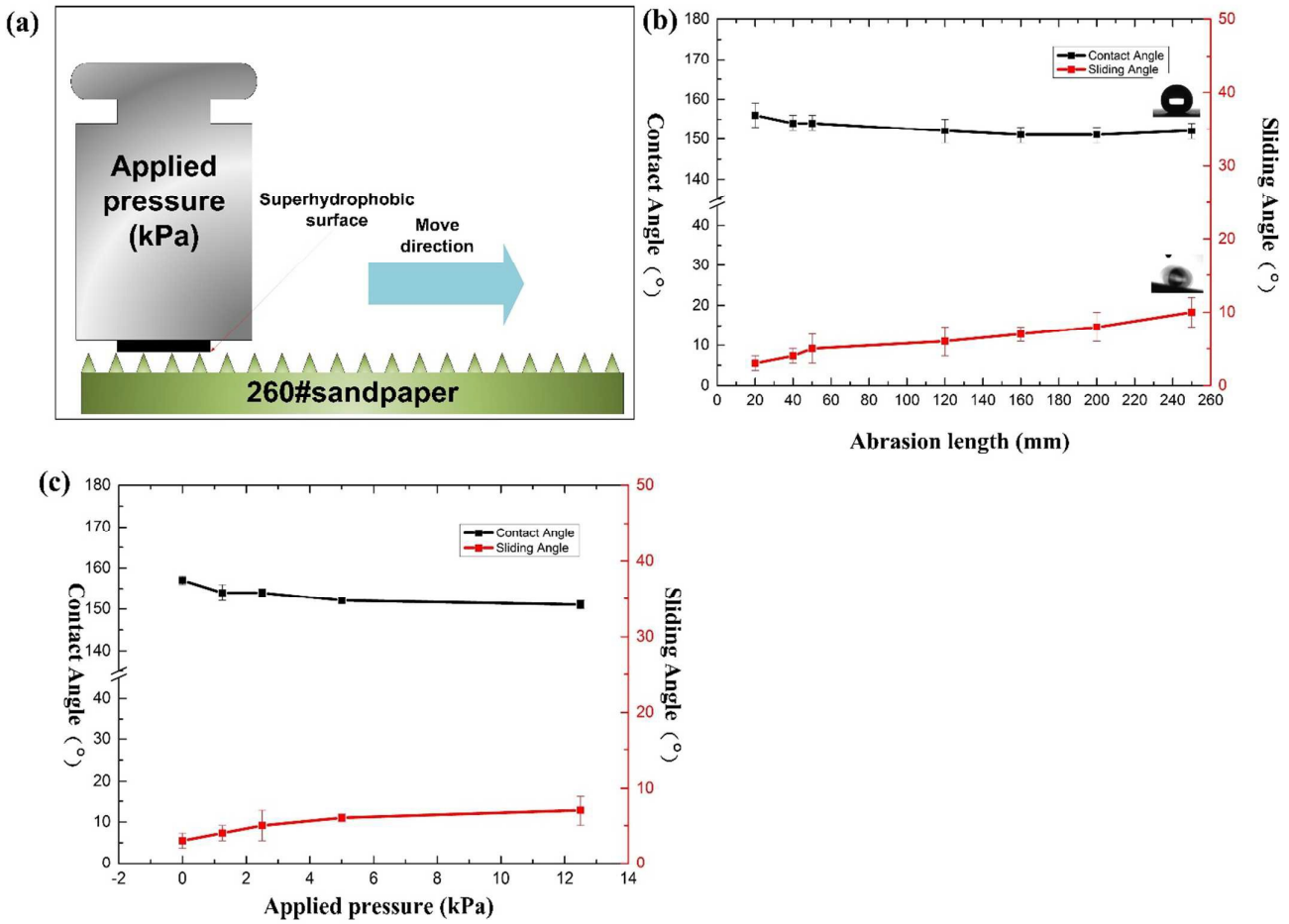

Figure. 9 (a) Illustration of the sandpaper abrasion test for A8 surface, (b) Contact angle and sliding angles of superhydrophobic surfaces with increasing abrasion length at the applied pressure of 12.5 kPa. (c) Contact angle and sliding angles of different structures superhydrophobic surface after abrasion 2.5 m at the applied pressure of 12.5 kPa..

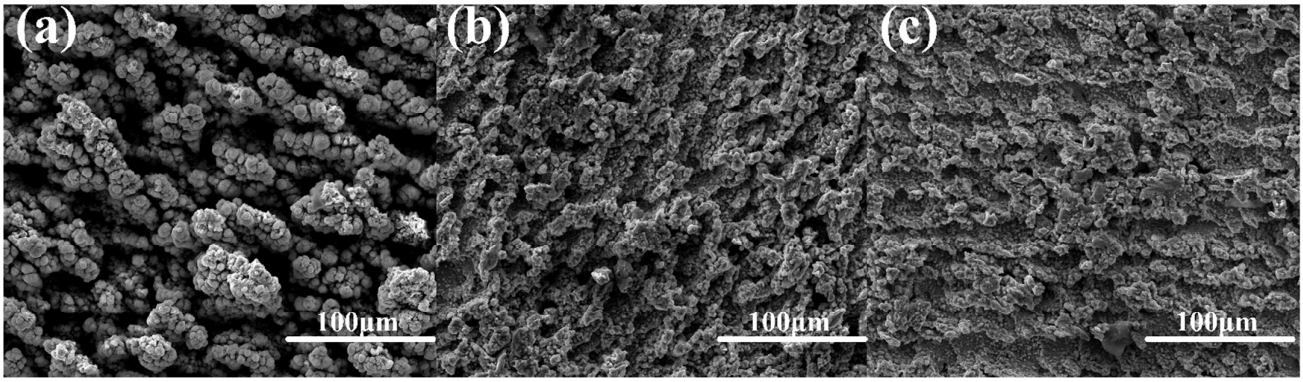

Figure. 10 SEM images of the abraded superhydrophobic surface, (a) before abrasion (b) after abrasion 1.0 m at the applied pressure of 12.5 kPa and (c) abrasion 2.5 m at the applied pressure of 12.5 kPa.

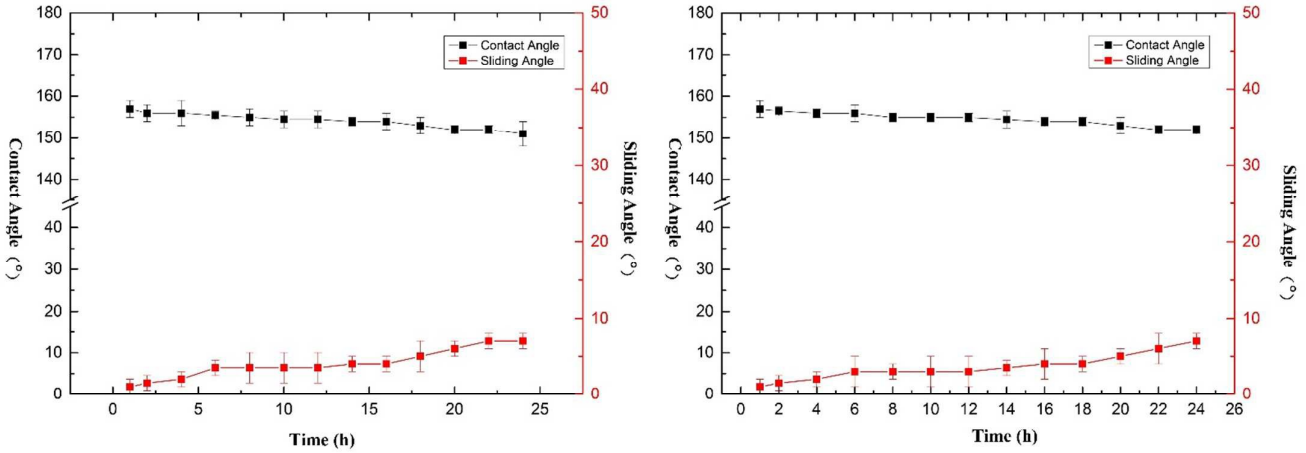

Figure. 11 Variation of the contact angle and sliding angle against time duration, (a) acidic solution (pH=1), (b) alkaline solution (pH=13).

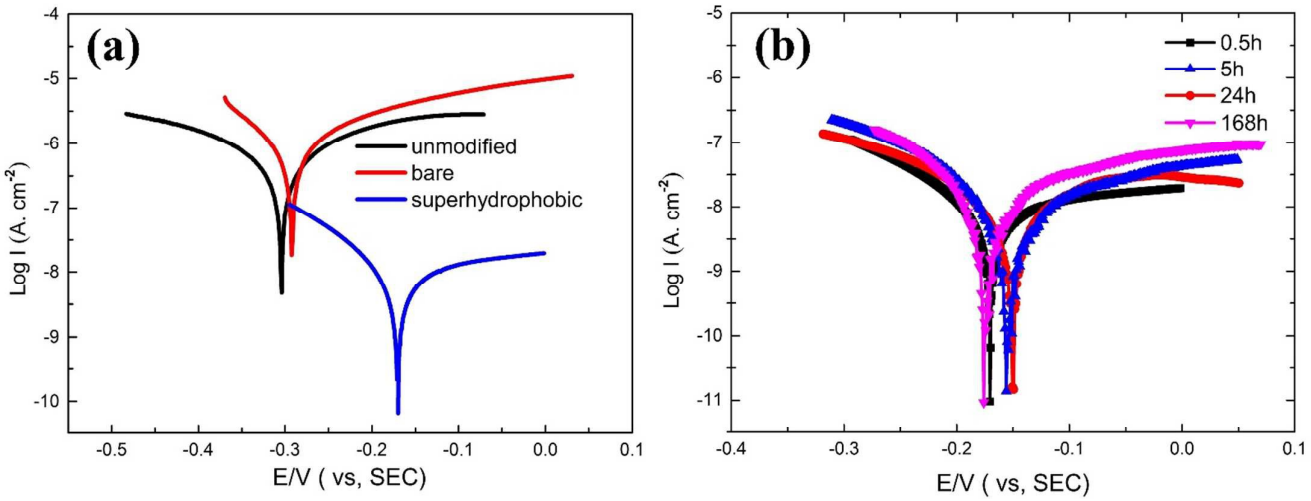

Figure. 12 (a) The Tafel polarization curves of bare stainless steel, unmodified laser processed sample and FAS-17 modified superhydrophobic sample. (b) Tafel polarization curves of the as-prepared superhydrophobic surfaces after 0.5h immersion (black line), 5h (blue line), 24h (red line) and 168 h (pink line) in 3.5 wt% NaCl aqueous solution.

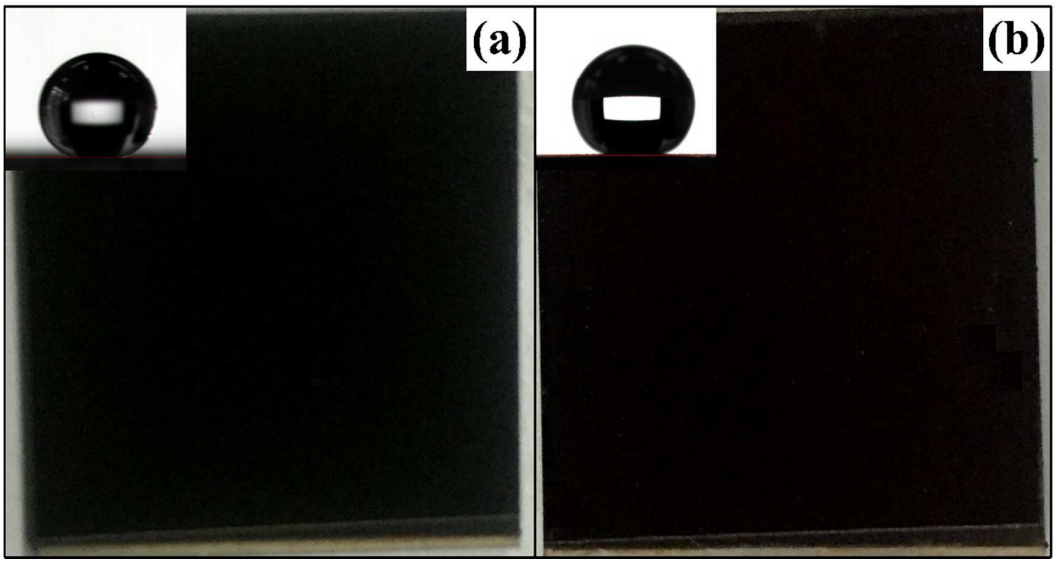

Figure.13 Salt fog exposure tests on the superhydrophobic surface, (a) pre-salt fog exposure, (b) 120h exposure.